

## Li<sub>10</sub>Ge(P<sub>1-x</sub>Sb<sub>x</sub>)<sub>2</sub>S<sub>12</sub> Lithium-Ion Conductors with Enhanced Atmospheric Stability

Jianwen Liang, Ning Chen, Xiaona Li, Xia Li, Keegan R. Adair, Junjie Li,  
Changhong Wang, Chuang Yu, Mohammad Norouzi Banis, Li Zhang, Shangqian  
Zhao, Shigang Lu, Huan Huang, Ruying Li, Yining Huang, and Xueliang Sun

*Chem. Mater.*, **Just Accepted Manuscript** • DOI: 10.1021/acs.chemmater.9b04764 • Publication Date (Web): 30 Jan 2020

Downloaded from [pubs.acs.org](https://pubs.acs.org) on February 3, 2020

### Just Accepted

“Just Accepted” manuscripts have been peer-reviewed and accepted for publication. They are posted online prior to technical editing, formatting for publication and author proofing. The American Chemical Society provides “Just Accepted” as a service to the research community to expedite the dissemination of scientific material as soon as possible after acceptance. “Just Accepted” manuscripts appear in full in PDF format accompanied by an HTML abstract. “Just Accepted” manuscripts have been fully peer reviewed, but should not be considered the official version of record. They are citable by the Digital Object Identifier (DOI®). “Just Accepted” is an optional service offered to authors. Therefore, the “Just Accepted” Web site may not include all articles that will be published in the journal. After a manuscript is technically edited and formatted, it will be removed from the “Just Accepted” Web site and published as an ASAP article. Note that technical editing may introduce minor changes to the manuscript text and/or graphics which could affect content, and all legal disclaimers and ethical guidelines that apply to the journal pertain. ACS cannot be held responsible for errors or consequences arising from the use of information contained in these “Just Accepted” manuscripts.

# Li<sub>10</sub>Ge(P<sub>1-x</sub>Sb<sub>x</sub>)<sub>2</sub>S<sub>12</sub> Lithium-Ion Conductors with Enhanced Atmospheric Stability

Jianwen Liang,<sup>†, ‡</sup> Ning Chen,<sup>‡, †</sup> Xiaona Li,<sup>†</sup> Xia Li,<sup>†</sup> Keegan R. Adair,<sup>†</sup> Junjie Li,<sup>†</sup> Changhong Wang,<sup>†</sup> Chuang Yu,<sup>†</sup> Mohammad Norouzi Banis,<sup>†</sup> Li Zhang,<sup>§</sup> Shangqian Zhao,<sup>§</sup> Shigang Lu,<sup>§</sup> Huan Huang,<sup>//</sup> Ruying Li,<sup>†</sup> Yining Huang,<sup>#</sup> and Xueliang Sun<sup>†,\*</sup>

<sup>†</sup> Department of Mechanical and Materials Engineering  
University of Western Ontario  
London, Ontario N6A 5B9, Canada  
E-mail: xsung@uwo.ca

<sup>‡</sup> Canadian Light Source  
44 Innovation Boulevard, Saskatoon, SK S7N 2V3, Canada

<sup>§</sup> China Automotive Battery Research Institute Co. Ltd  
5th Floor, No. 43, Mining Building, North Sanhuan Middle Road, Beijing, China

<sup>//</sup> Glabat Solid-State Battery Inc.  
700 Collip Circle, London, ON, N6G 4X8, Canada

<sup>#</sup> Department of Chemistry  
University of Western Ontario  
1151 Richmond St, London, Ontario, N6A 3K7, Canada

---

**ABSTRACT:** Sulfide solid electrolytes have recently attracted significant interest for use in all-solid-state lithium batteries (ASSLBs) due to their high ionic conductivity. However, one of the main challenges associated with the commercialization of sulfide-based electrolytes is their instability toward air/moisture, which leads to complex processing requirements. Herein, we develop a strategy to not only increase ionic conductivity but also obtain high air-stability of the Li<sub>10</sub>Ge(P<sub>1-x</sub>Sb<sub>x</sub>)<sub>2</sub>S<sub>12</sub> electrolyte system with soft acid Sb substitution. Theoretical calculations predict the Sb substitution in (Ge,P)<sub>4</sub> tetrahedral sites, which is further confirmed by the X-ray diffractions Rietveld refinement and synchrotron X-ray absorption fine structure analysis. Opened channels and increased unit cell volume are achieved with an appropriate amount of Sb substitution, leading to an ultra-high ionic conductivity of 17.3 ± 0.9 mS cm<sup>-1</sup>. The softer acidity of Sb compared to P also ensures strong covalent bonding with S in Li<sub>10</sub>Ge(P<sub>1-x</sub>Sb<sub>x</sub>)<sub>2</sub>S<sub>12</sub> which improves the air stability of the electrolyte. Moreover, the air-exposed samples exhibit high ionic conductivities of 12.1-15.7 mS cm<sup>-1</sup>. Bulk-type ASSLBs assembled with either pristine or air-exposed Li<sub>10</sub>Ge(P<sub>1-x</sub>Sb<sub>x</sub>)<sub>2</sub>S<sub>12</sub> exhibit high initial Coulombic Efficiencies of 92.8% and 91.0%, respectively, with excellent cycling performance over 110 cycles. The observed variations in the structural parameters and bond strength provide an effective approach toward designing more ionically conductive and stable solid-state electrolytes.

---

## INTRODUCTION

Solid-state electrolytes (SSEs) are key materials in all-solid-state lithium batteries (ASSLBs) because of their ionic conductivity, wide electrochemical window, stability and other parameters of SSEs dominate the performance

and assembling of ASSLBs.<sup>1-5</sup> Compared to other types of SSEs including oxide, polymer, halide, and borohydride materials, sulfide SSEs are quite promising due to their intrinsically high ionic conductivity (even over 10 mS cm<sup>-1</sup>) and deformability.<sup>6-10</sup> Among the various reported sulfide

SSEs,  $\text{Li}_{10}\text{GeP}_2\text{S}_{12}$  has emerged as one of the most promising candidates due to its ultra-high ionic conductivity of  $12 \text{ mS cm}^{-1}$ ,<sup>6</sup> and successful application in ASSLBs.<sup>11-13</sup> However, like most of the other sulfide SSEs,  $\text{Li}_{10}\text{GeP}_2\text{S}_{12}$  is quite air/moisture sensitive, leading to toxic  $\text{H}_2\text{S}$  generation when exposed to an ambient environment, and thus limiting its practical application.<sup>14,15</sup> Moreover, the ionic conductivity of sulfide SSEs after air/moisture exposure would be reduced by several orders of magnitude, making it impractical for industrial use.<sup>16</sup>

Based on the hard and soft acids and bases (HSAB) theory,<sup>17</sup> the hard acid of  $\text{P}^{5+}$  within  $\text{Li}_{10}\text{GeP}_2\text{S}_{12}$  tends to bond with oxygen in air/moisture to form P-O bonds rather than maintaining the pristine P-S bonding structure. Simultaneously, sulfur atoms tend to bond with the hydrogen in air/moisture, leading to the release of  $\text{H}_2\text{S}$ .<sup>18</sup> Comparatively, Ge-S bonds within  $\text{Li}_{10}\text{GeP}_2\text{S}_{12}$  are more stable, due to the strong bonding between the soft acid of  $\text{Ge}^{4+}$  and the soft base of  $\text{S}^{2-}$ . Similar interaction has also been proved effective in other battery systems.<sup>19,20</sup> Therefore, total or partial substitution of P content in the  $\text{Li}_{10}\text{GeP}_2\text{S}_{12}$  is necessary to achieve air/moisture stability. Huang et al. have recently shown the development of a new  $\text{Li}_3\text{Cu}_8\text{Ge}_3\text{S}_{12}$  SSE based on HSAB theory which exhibits good stability toward moisture. Nevertheless, the main drawbacks of this new SSE are the relatively low ionic conductivity ( $< 1 \times 10^{-4} \text{ S cm}^{-1}$ ) and low decomposition voltage (1.5 V).<sup>21</sup>

Among the potential elements, Sb is one of the most promising substitution candidates.<sup>22,23</sup> While it belongs to the same group of P, Sb is a much softer acid compared to P.<sup>17</sup> The rigid covalent bonding between Sb and S has a low affinity towards oxygen, which has been proved by the existence of hydrated  $\text{Na}_3\text{SbS}_4 \cdot x\text{H}_2\text{O}$  for typical  $\text{Na}_3\text{SbS}_4$  SSE rather than decomposition of  $\text{Na}_3\text{SbS}_4$ .<sup>18,24,25</sup> Furthermore, the larger ionic radius of Sb ( $r_{\text{P}^{5+}} = 38 \text{ pm}$ ,  $r_{\text{Sb}^{5+}} = 60 \text{ pm}$ )<sup>26</sup> is expected to broaden the  $\text{Li}^+$  diffusion pathways. Theoretically, the incorporation of larger  $\text{Sb}^{5+}$  into  $\text{Li}_{10}\text{GeP}_2\text{S}_{12}$  is predicted to change the local environment, especially the two types of  $(\text{Ge,P})\text{S}_4$  and  $\text{PS}_4$  tetrahedra as well as the total volume of the unit cells. Moreover, the lower electronegativity of Sb is beneficial in reducing the corresponding binding energy of  $\text{S}^{2-}$  to  $\text{Li}^+$  in the framework, which would further promote high ionic conductivity.<sup>27,28</sup>

In this work, inspired by the possibility of incorporating Sb into  $\text{Li}_{10}\text{GeP}_2\text{S}_{12}$  to promote air/moisture stability and a larger unit cell, we investigated the effect of  $\text{Sb}^{5+}$  substitution in  $\text{Li}_{10}\text{Ge}(\text{P}_{1-x}\text{Sb}_x)_2\text{S}_{12}$  electrolytes ( $0\% \leq x \leq 100\%$ ). With appropriate Sb content ( $x \leq 12.5\%$ ), volume expansion, as well as open channels, are induced and thus faster  $\text{Li}^+$  migration is guaranteed. Beyond this range, secondary phases will be formed rather than incorporating Sb. An ultra-high room-temperature ionic conductivity of  $17.3 \pm 0.9 \text{ mS cm}^{-1}$  was achieved for  $\text{Li}_{10}\text{Ge}(\text{P}_{0.925}\text{Sb}_{0.075})_2\text{S}_{12}$ . Furthermore, X-ray Rietveld refinement and theoretical calculation combined with synchrotron X-ray absorption fine structure fitting confirmed that the position of the Sb

substitution is in the  $4d$  P site in the center of  $(\text{Ge,P})\text{S}_4$  tetrahedra, leading to high stability against air/moisture with an ionic conductivity of  $12.1\text{-}15.7 \text{ mS cm}^{-1}$  being retained for air-exposed samples. Sb substitution is proved as an effective strategy to design sulfide SSEs with both superionic conductivity and air stability towards further practical application.

## EXPERIMENTAL SECTION

**Synthesis.** The  $\text{Li}_{10}\text{Ge}(\text{P}_{1-x}\text{Sb}_x)_2\text{S}_{12}$  solid electrolytes were synthesized using a solid-state reaction. The starting materials were  $\text{Li}_2\text{S}$  (Alfa Aesar, >99.9% purity),  $\text{P}_2\text{S}_5$  (Sigma-Aldrich, >99% purity),  $\text{Sb}_2\text{S}_5$  (Sigma-Aldrich,  $\geq 60\%$  Sb basis), and  $\text{GeS}_2$  (Sigma-Aldrich, >99% purity). These reagents were weighed in the molar ratio of  $\text{Li}_2\text{S}/\text{P}_2\text{S}_5/\text{Sb}_2\text{S}_5/\text{GeS}_2$  to  $10/(1-x)/x/1$  in an Ar-filled glove box. Here the data of  $x$  was 0.01 to 1. The weighted samples were placed into a  $\text{ZrO}_2$  pot with  $\text{ZrO}_2$  balls ( $\phi 10 \text{ mm}$ ) and mechanically milled using the planetary ball milling apparatus at 400 rpm for 12 h. After 12 h, the sample was scraped down from the  $\text{ZrO}_2$  pot and then mechanically milled again for 12 h at 400 rpm. The product mixtures were then pressed into pellets under 360 MPa, sealed in quartz tube at  $\sim 100 \text{ Pa}$ , and treated at  $475 \text{ }^\circ\text{C}$  (heated from  $25 \text{ }^\circ\text{C}$  to  $475 \text{ }^\circ\text{C}$  in 4 h) for 24 h in a furnace. Then the tubes were cooled to room temperature for 4 h.

**Characterization.** X-ray diffraction patterns of the synthesized powders were collected using an X-ray diffractometer (Bruker AXS D8) with  $\text{Cu K}\alpha$  radiation ( $\lambda = 1.54178 \text{ \AA}$ ). The diffraction data were collected at one step of  $0.02^\circ$  over a  $2\theta$  range from  $10$  to  $80^\circ$ . The data for the X-ray refinement were collected on Bruker AXS D8 Advance with a  $\text{Cu K}\alpha$  radiation. The data were collected by scanning  $5\text{ s}$  per step with one step of  $0.02^\circ$  from  $10$  to  $90^\circ$  ( $2\theta$ ). The samples were loaded to an airtight specimen holder (Figure S1) for XRD test to avoid air exposure. After sealing, the holder loaded with the sample was transferred from the glovebox to the XRD machine for tests. Transmission electron microscopy (TEM) analysis was performed on a JEM-2100 Electron Microscope (JEM-2100, 200 kV). X-ray refinement was performed by the software of Accelrys Material Studio. Solid-state NMR experiments were performed on a Varian Infinity Plus 400 (I+400) NMR spectrometer (7.5 T). A commercial resonance 5 mm MAS probe was used at Larmor frequencies of  $155.248 \text{ MHz}$  for  $^7\text{Li}$ . The temperature range for  $^7\text{Li}$  SLR NMR is  $303 \text{ K}$  to  $443 \text{ K}$ . The  $^7\text{Li}$  chemical shifts were referenced to  $\text{LiCl}$  (0.1 M a.q.). For the  $\text{H}_2\text{S}$  generation tests, powder samples (350 mg) and an  $\text{H}_2\text{S}$  gas sensor (968-021 SDK- $\text{H}_2\text{S}$  SENSOR DEVELOPER, SPEC Sensors, LLC.) were placed in a sealed container ( $18600 \text{ cm}^3$ ) filled with humid air (humidity around 1-3%). The humidity was controlled by using desiccating agents ( $\text{CaCl}_2$ , silica gel, etc.) combined with a saturated  $\text{CsF}$  solution in a  $\sim 50 \text{ L}$  box equipped with a humidity sensor. The humidity of the saturated  $\text{CsF}$  solution is 4.3% at room temperature. Firstly, fresh ambient air was dehydrated using silica gel and  $\text{CaCl}_2$ . Then the dehydrated air was flowed into the saturated  $\text{CsF}$  solution to make a low humidity airflow (humidity around

5%). After that, the low humidity airflow was mixed with dry air by the ratio of 1:1 and then flow into the 50 L box. Antimony (Sb) K-edge X-ray absorption fine structure (XAFS) data were collected at Hard X-ray MicroAnalysis (HXMA) beamline of the Canadian Light Source (CLS) with samples covered with Kapton tape to avoid air exposure.<sup>29</sup> During the measurement, CLS storage ring was operated under 220 mA operation mode.

**Computational section:** Density functional theory (DFT) calculations were performed to theoretically investigate the possible Sb substitution sites in the  $\text{Li}_{10}\text{GeP}_2\text{S}_{12}$  structure (Sb-LGPS) based on the total energy. The calculation was conducted to both static computation and geometry optimization of  $\text{Li}_{10}\text{Ge}(\text{P}_{1-x}\text{Sb}_x)_2\text{S}_{12}$  using the CASTEP DFT code of Accelrys Material Studio with the exchange-correlation functional of Perdew-Burke-Ernzerh (PBE) based on generalized gradient approximation (GGA). The cut-off energy for the plane-wave basis is set as 330.0 eV. The k-point mesh of  $3^*3^*1$  is adopted and the SCF tolerance is set as  $5.0^*10^{-7}$  eV  $\text{\AA}^{-1}$ . The atomic positions and cell parameters are fully relaxed to obtain total energy and optimized cell structure. Five models were built. The first model was LGPS without any substitution of  $\text{Sb}_p$ . The second model was built by  $\text{Sb}_p$  in *2b* site with full occupation, the third model was built by fully occupation of  $\text{Sb}_p$  in *4d* site, and the forth model was built by half of occupation of  $\text{Sb}_p$  in both the two P sites, all with totally half of P sites were substituted by Sb in the structure. Thus, there were same Sb concentration in the structures for the 2<sup>nd</sup> model to the 4<sup>th</sup> model. The last model was built by all of the P sites occupied by Sb, which means no P atom in this structure. The  $\text{Sb}_p$  formation energy was calculated by using the equation as follow,  $\text{LGPS} + x\text{Sb} = x\text{Sb-LGPS} + x\text{P}$ . Then,  $E = E_{(x\text{Sb-LGPS})} + x^*E_{\text{P}} - E_{(\text{LGPS})} - x^*E_{\text{Sb}}$ .

**Ionic and electronic conductivities.** The ionic conductivity was measured performed on the versatile multichannel potentials at 3/Z (VMP3, Biologic) by applying an AC voltage of 10 mV amplitude in the 7 MHz to 1 Hz frequency range. The  $\text{Li}_{10}\text{Ge}(\text{P}_{1-x}\text{Sb}_x)_2\text{S}_{12}$  powder was pressed at 360 MPa to form a pellet (diameter 10 mm,

thickness about 1 mm) in an Ar atmosphere glove box. Then,  $\text{Li}_{10}\text{Ge}(\text{P}_{1-x}\text{Sb}_x)_2\text{S}_{12}$  pellets were heated at 475 °C for 4 h and cooled to room temperature naturally. Then those pellets were attached with indium foil on both sides at 70 MPa for ionic conductivity test. The impedance of symmetric  $\text{In}/\text{Li}_{10}\text{Ge}(\text{P}_{1-x}\text{Sb}_x)_2\text{S}_{12}/\text{In}$  cells was measured between -65 and 25 °C. Each temperature is waiting for one hour before being measured. The electrical conductivity was investigated by using symmetric  $\text{In}/\text{Li}_{10}\text{Ge}(\text{P}_{1-x}\text{Sb}_x)_2\text{S}_{12}/\text{In}$  cells with different applied voltages (0.1, 0.2 and 0.3 V) for 1 h.

**Charge-discharge measurements.** Bulk-type all-solid-state cells ( $\text{LiCoO}_2/\text{Li}_{10}\text{Ge}(\text{P}_{1-x}\text{Sb}_x)_2\text{S}_{12}$  electrolyte/ $\text{In}$ ) were fabricated as follows. Commercial  $\text{LiCoO}_2$  (99.8% trace metals basis) powders were purchased from Sigma-Aldrich.  $\text{LiNbO}_x$ -coated  $\text{LiCoO}_2$  particles by atomic layer deposition (ALD) method were used as positive electrodes to avoid undesirable side reactions based on our previous study.<sup>30,31</sup>  $\text{LiNbO}_x$ -coated  $\text{LiCoO}_2$  particles and the  $\text{Li}_{10}\text{Ge}(\text{P}_{1-x}\text{Sb}_x)_2\text{S}_{12}$  electrolytes with the weight ratio of 70:30 were mixed using a pot mill rotator (U.S. Stoneware, No. cz-17018) for 10 min to prepare a composite positive electrode. There is no conductive carbon additive included in the cathode part. An indium foil (Sigma-Aldrich, purity 99.9%) was used as a negative electrode.  $\text{Li}_{10}\text{Ge}(\text{P}_{1-x}\text{Sb}_x)_2\text{S}_{12}$  electrolyte (80 mg) was firstly pressed at 240 MPa to form a pellet (10 mm diameter). Then the composite positive electrode (10 mg) was uniformly spread onto the surface of the electrolyte and pressed at 360 MPa to form a bi-layer pellet. Then indium foil was attached to the other side of the bi-layer pellet by pressing at 120 MPa. The pellet was pressed by two stainless steel rods. All processes for preparing the cathode composites and fabricating the all-solid-state cells were performed in a dry Ar-filled glove box. The electrochemical properties of the cells were determined using a Land cyler (Wuhan, China). The cycling test was carried out between 1.90-3.60 V vs.  $\text{Li}^+/\text{LiIn}$  at 100 mA  $\text{g}^{-1}$  at room temperature.

## RESULTS AND DISCUSSION

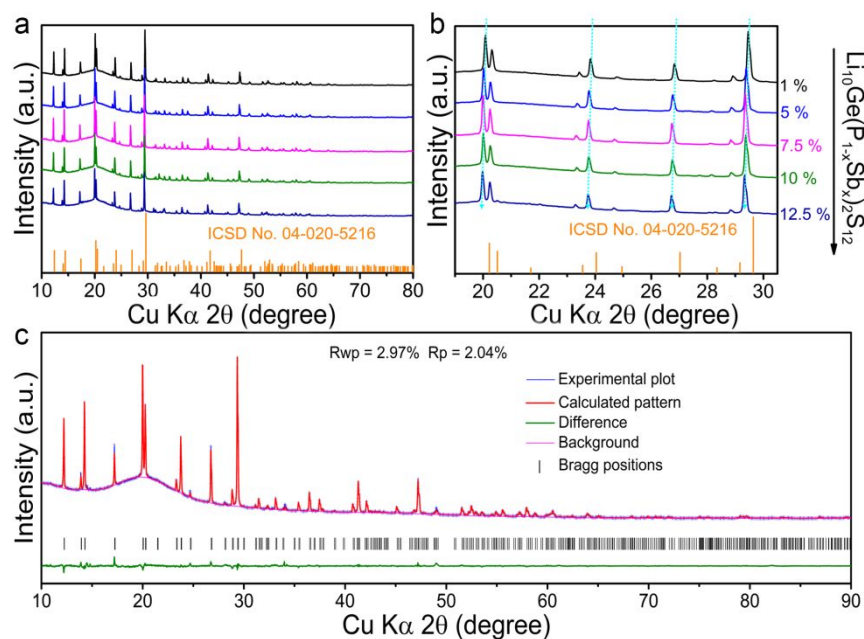


**Figure 1.** XRD and structure analysis of  $\text{Li}_{10}\text{Ge}(\text{P}_{1-x}\text{Sb}_x)_2\text{S}_{12}$ . (a,b) XRD patterns of  $\text{Li}_{10}\text{Ge}(\text{P}_{1-x}\text{Sb}_x)_2\text{S}_{12}$  samples with different degrees of Sb incorporation ( $x = 0.01, 0.05, 0.075, 0.1, \text{ and } 0.125$ ). (c) Representative XRD pattern of  $\text{Li}_{10}\text{Ge}(\text{P}_{0.925}\text{Sb}_{0.075})_2\text{S}_{12}$  and the corresponding Rietveld refinement. Rwp and Rp are the weighted profile R-factor and goodness of fit, respectively.

$\text{Li}_{10}\text{Ge}(\text{P}_{1-x}\text{Sb}_x)_2\text{S}_{12}$  with different degrees of SbThe  $\text{Li}_{10}\text{Ge}(\text{P}_{1-x}\text{Sb}_x)_2\text{S}_{12}$  ( $0 \leq x \leq 100\%$ ) SSEs were synthesized by reacting stoichiometric quantities of  $\text{Li}_2\text{S}$ ,  $\text{GeS}_2$ ,  $\text{P}_2\text{S}_5$ , and  $\text{Sb}_2\text{S}_5$  at  $475^\circ\text{C}$  in an evacuated and sealed quartz tube (detailed procedure can be found in the supporting information). X-ray diffraction (XRD) patterns (the airtight specimen holder as presented in Figure S1) of incorporation were firstly obtained to study the structural variations. The XRD patterns of the samples were compared in Figure 1a, b, and S2. The XRD pattern can be indexed with  $\text{Li}_{10}\text{GeP}_2\text{S}_{12}$  ( $P4_2/nmc$ , ICSD No. 04-020-5216)<sup>32</sup> when the Sb substitution content is lower than 12.5% (Figure 1a). Moreover, the XRD peaks associated with the synthesized  $\text{Li}_{10}\text{Ge}(\text{P}_{1-x}\text{Sb}_x)_2\text{S}_{12}$  ( $0 \leq x \leq 12.5\%$ ) shift to a lower angle compared to the pristine  $\text{Li}_{10}\text{GeP}_2\text{S}_{12}$ , as presented in Figure 1b. The lower angle shift is more obvious with an increase of Sb content, demonstrating the expansion of the unit cell volume. Thus, it can be concluded the successful substitution of Sb into the  $\text{Li}_{10}\text{GeP}_2\text{S}_{12}$  structure. Nevertheless, impurity peaks at  $2\theta = 18.3, 18.9, 30.02, 47.96, \text{ and } 48.10^\circ$  emerged when the Sb content was higher than 12.5% (Figure S2). The corresponding intensity of these impurity peaks increased along with an increase of Sb content in the  $\text{Li}_{10}\text{Ge}(\text{P}_{1-x}\text{Sb}_x)_2\text{S}_{12}$  SSEs, indicating that the introduction of too much Sb will lead to the destruction of the  $\text{Li}_{10}\text{GeP}_2\text{S}_{12}$  structure. This should be due to the larger ionic radius of  $\text{Sb}^{5+}$  (60 pm) compared to  $\text{P}^{5+}$  (38 pm) and  $\text{Ge}^{4+}$  (53 pm).

The detailed structures of  $\text{Li}_{10}\text{Ge}(\text{P}_{1-x}\text{Sb}_x)_2\text{S}_{12}$  have been studied by XRD Rietveld refinement, Density functional theory (DFT) calculation and X-ray absorption fine structure (XAFS) fitting. Typical XRD of  $\text{Li}_{10}\text{Ge}(\text{P}_{0.925}\text{Sb}_{0.075})_2\text{S}_{12}$  (Sb substitution content is 7.5%) and the corresponding Rietveld refinement<sup>33,34</sup> are shown in Figure 1c. At the same time, related structure information of  $\text{Li}_{10}\text{Ge}(\text{P}_{0.925}\text{Sb}_{0.075})_2\text{S}_{12}$  are shown in Figure S3 and Table S1.  $\text{Li}_{10}\text{Ge}(\text{P}_{0.925}\text{Sb}_{0.075})_2\text{S}_{12}$  presents a slightly different structure compared to that of  $\text{Li}_{10}\text{GeP}_2\text{S}_{12}$  in the database (the crystal structure and unit cell parameters are shown in Figure S4 and Table S2). Crystallographic studies of  $\text{Li}_{10}\text{GeP}_2\text{S}_{12}$  have identified two distinct P sites, namely, the  $4d$  and  $2b$  sites. The  $2b$  site is fully occupied by P forming a  $\text{PS}_4$  tetrahedron; while the  $4d$  site is occupied by not only P but also Ge forming a  $(\text{Ge,P})\text{S}_4$  tetrahedron.<sup>6,35</sup> The occupancy parameter of P and Ge is 0.5. Different from  $\text{Li}_{10}\text{GeP}_2\text{S}_{12}$ , the introduced Sb in  $\text{Li}_{10}\text{Ge}(\text{P}_{0.925}\text{Sb}_{0.075})_2\text{S}_{12}$  shares the  $4d$  site together with P and Ge, forming a  $(\text{P,Ge,Sb})\text{S}_4$  tetrahedron with different P, Ge, and Sb occupancy, as shown in Figure S3. Moreover, Sb substitution in  $\text{Li}_{10}\text{GeP}_2\text{S}_{12}$  also leads to changes in the unit cell parameters (Table S3). Compared to the pristine  $\text{Li}_{10}\text{GeP}_2\text{S}_{12}$ , both the  $a, c$  axis as well as the unit cell volume increased for  $\text{Li}_{10}\text{Ge}(\text{P}_{0.925}\text{Sb}_{0.075})_2\text{S}_{12}$ . The increased  $a, c$  axis and the unit cell volume are believed to be beneficial to the  $\text{Li}^+$  migration since both the  $\text{Li}^+$  migration within the  $ab$  plane and the ultra-fast  $\text{Li}^+$  migration along the  $c$  direction has been reported.<sup>6,36</sup>

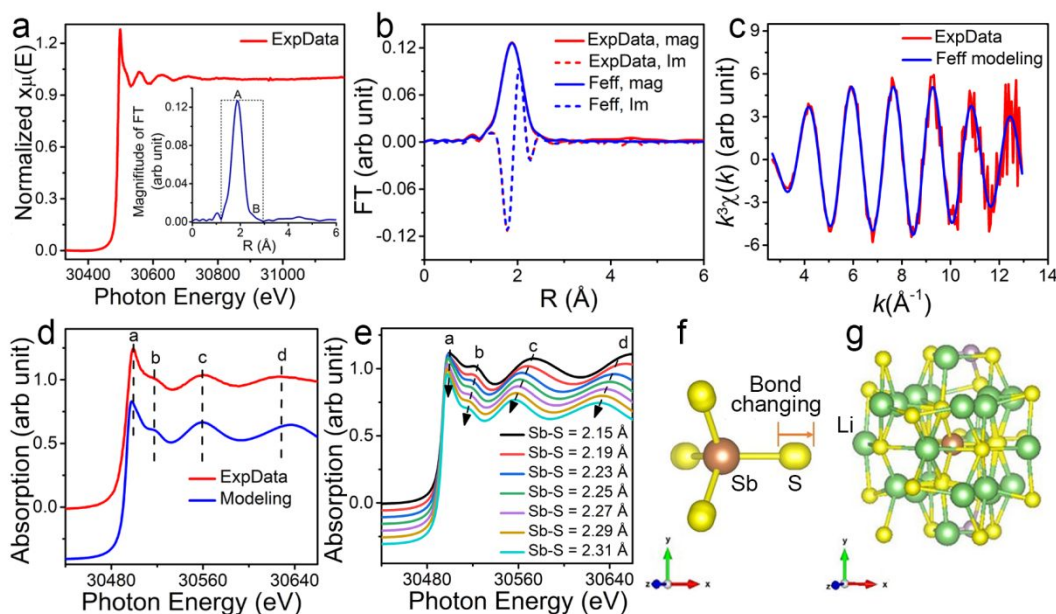


**Figure 2.**  $Sb_P$  local environment based on XAFS fitting. (a) Sb K-edge XAFS spectroscopy of  $Li_{10}Ge(P_{0.925}Sb_{0.075})_2S_{12}$ . Inset, the magnitude of FT for  $k^3\chi(k)$  of the experimental data and experimentally resolved EXAFS features “A” and “B”. (b) The magnitude and imaginary part of FT between the experimental (red solid and red dash traces) and the Feff modeling (blue solid and blue dash traces) of  $Sb_P$  in  $4d$  with 7.5% substitution. (c)  $k^3\chi(k)$  between the experimental and the Feff modeling of  $Sb_P$  in  $4d$  with 7.5% substitution based on the R space curve fitting result. (d) Comparison between the experimental XANES (red line) and the best fit of the XANES theoretical modeling (blue line). (e) The resulted theoretical XANES system based on the developed structural system with different bond lengths of Sb-S in  $SbS_4$  tetrahedra. (f) The first shell of the  $SbS_4$  sub-structural system. The orange arrow indicates the direction and the scale of the changing trend for Sb-S bonding. (g) The complete structural system carried out by  $SbS_4$  sub-structural system.

DFT calculations were further performed to theoretically investigate the Sb substitution sites ( $Sb_P$ ) in the  $Li_{10}GeP_2S_{12}$  structure. There are four kinds of possible substitution situations:  $Sb_P$  in  $2b$  site,  $Sb_P$  in  $4d$  site,  $Sb_P$  in half of  $2b$  and  $4d$  sites, and  $Sb_P$  in both  $2b$  and  $4d$  sites. Therefore, five structures were calculated by DFT modeling: 1) pristine  $Li_{10}GeP_2S_{12}$ , denoted as LGPS; 2) Sb substitute P atom in  $2b$  site of  $Li_{10}GeP_2S_{12}$ , denoted as LGPS-Sb ( $2b$ ); 3) Sb substitute P atom in  $4d$  site of  $Li_{10}GeP_2S_{12}$ , denoted as LGPS-Sb ( $4d$ ); 4) Sb substitute half of P in  $4d$  and  $2b$  sites of  $Li_{10}GeP_2S_{12}$ , denoted as LGPS-Sb (half); and 5) completely substitution of P by Sb both in the  $4d$  and  $2b$  sites, denoted as LGPS-Sb (all). The  $Sb_P$  formation energies of LGPS without any Sb substitution was set as 0 eV. The  $Sb_P$  formation energies of the other structures were compared in Figure S5. The  $Sb_P$  in  $2b$  site will result in a higher energy of +0.8 eV, indicating that Sb substitution in this location is not favored considering the preferred lower energy of the system. However, Sb substitution in  $4d$  and half of  $4d/2b$  sites leads to lower energies of -19.44 and -18.76 eV, respectively. Thus, it can be concluded that introducing Sb into  $Li_{10}GeP_2S_{12}$  results in the preferred substitution of P atoms in the  $4d$  site. The conclusion from DFT calculations is in good agreement with the Rietveld refinement results. Moreover, complete substitution of both P atoms in  $Li_{10}GeP_2S_{12}$  while maintaining the LGPS structure is not possible considering the high energy of +155.3 eV. This is consistent with the XRD results in Figure S2 which show

that the obtained structure is completely different from the pristine  $Li_{10}GeP_2S_{12}$  when  $x = 100\%$ .

Sb K-edge XAFS spectroscopy has been further employed to reveal the local environment of Sb in  $Li_{10}Ge(P_{0.925}Sb_{0.075})_2S_{12}$  sample (Figure 2a). The XAFS models were developed based on the theoretical DFT modeling of 7.5%  $Sb_P$  in different positions of the LGPS structure. There are three models, which are  $Sb_P$  in  $2b$ ,  $4d$ , and half of  $2b/4d$  site (similar to the 2<sup>nd</sup> to the 4<sup>th</sup> model in Figure S5). The nearest neighbor Sb local environment is reflected by extended X-ray absorption fine structure (EXAFS) to the experimentally resolved first shell Fourier transform (FT) peak, peaking at around 1.87 Å and featured by its major feature “A” and a shoulder feature “B” on the high R side of the FT peak (inset of Figure 2a). The DFT modeled Sb local environment was used for Feff theoretical scattering amplitudes and phases calculation,<sup>37</sup> further for guiding EXAFS R space curve fitting. The XAFS data reduction and the followed R space curve fitting were performed by ATHENA software<sup>38</sup> and WINXAS<sup>39</sup>, respectively. The first inflection point of the Sb K-edge X-ray absorption near edge structure (XANES) was defined as the experimental  $E_0$ , the post-absorption edge background was estimated by cubic spline fits. The Gaussian window function was used for FT over the  $k$  range of 2.7–12.9 Å<sup>-1</sup> for  $k^3\chi(k)$  with a window parameter of 30%. The Feff R space fitting result and the experimental data presented in Figure 2b reveal an overall matching in both magnitude and

imaginary part of the FT. The good consistency is further observed in the  $k$  space for  $k^3\chi(k)$  between the experimental and the Feff modeling based on the R space curve fitting result (Figure 2d), proving that  $\text{Sb}_p$  in  $4d$  with 7.5% substitution is the most perfect structure for the fitting of the Sb K-edge XAFS spectroscopy (Figure 2c). The fitted parameters are summarized in Table S4. The EXAFS result clearly supports the DFT prediction regarding the  $\text{Sb}_p$  site in  $4d$  and its low occupancy.

Moreover, XANES theoretical modeling analysis was used to address the Sb local environment throughout experimentally resolved XANES features “a” to “d” (red line, Figure 2d). XANES modeling performed in two cycles was guided by the DFT model and EXAFS result obtained through R space curve fitting (Table S4).<sup>40</sup> The first XANES modeling was performed over a Sb centered spherical cluster (radius of 6 Å) generated by DFT model, which has successfully reproduced all experimentally resolved XANES features (Figure S6) and is consistent with the observation by EXAFS to support the Sb site occupancy predicted by DFT. To proceed the second cycle of XANES modeling, a Sb centered structural system was developed based on the cluster used for the first XANES modeling cycle with following further structural constraints: (a) the overall Sb local framework follows the DFT prediction; (b) guided by the EXAFS, the  $\text{SbS}_4$  tetrahedra were progressively enlarged with Sb-S bond from 2.15 Å (predicted by DFT) to 2.31 Å (Figure 2f) until the XANES best fit was identified (blue line, Figure 2d); (c) no local

environment adjustment was induced beyond the first shell  $\text{SbS}_4$  tetrahedral coordination (Figure 2g). The resulted theoretical XANES system based on the developed structural system (Figure 2e) reveals that XANES data trends “a” to “d” relate to the progressive changing of the Sb local environment. The XANES best fit was obtained with the first shell Sb-S bond distance adjusted to 2.27 Å, resulting in accurate reproducing the all experimentally resolved XANES features (Figure 2d).

Experimentally resolved XAFS features (Figure 2a,d) have all been addressed by the EXAFS R space curve fitting (Figure 2b,c, Table S4) and XANES theoretical modeling (Figure 2d-f, S6), supporting the DFT predicted Sb  $4d$  site occupancy. The Sb-S bond distance obtained by DFT, EXAFS, and XANES is 2.15, 2.34 (Table S4), and 2.27 Å, respectively, indicating that the Sb-S bond distance predicted by DFT is slightly underestimated by EXAFS and XANES. The XAFS revealed an underestimation trend by DFT is expected considering that the geometry of the  $4d$  site predicted by DFT is an averaged structure throughout bonds of Sb-S, Ge-S, and P-S, respectively. The Sb-S bond distance estimated by EXAFS is slightly longer than that determined from XANES modeling by 0.07 Å, which should be more accurate, considering the good quality of the EXAFS data as well as the R spacing curve fitting (Figure 2a,b) and the not considered structural defect effect on XANES modeling.

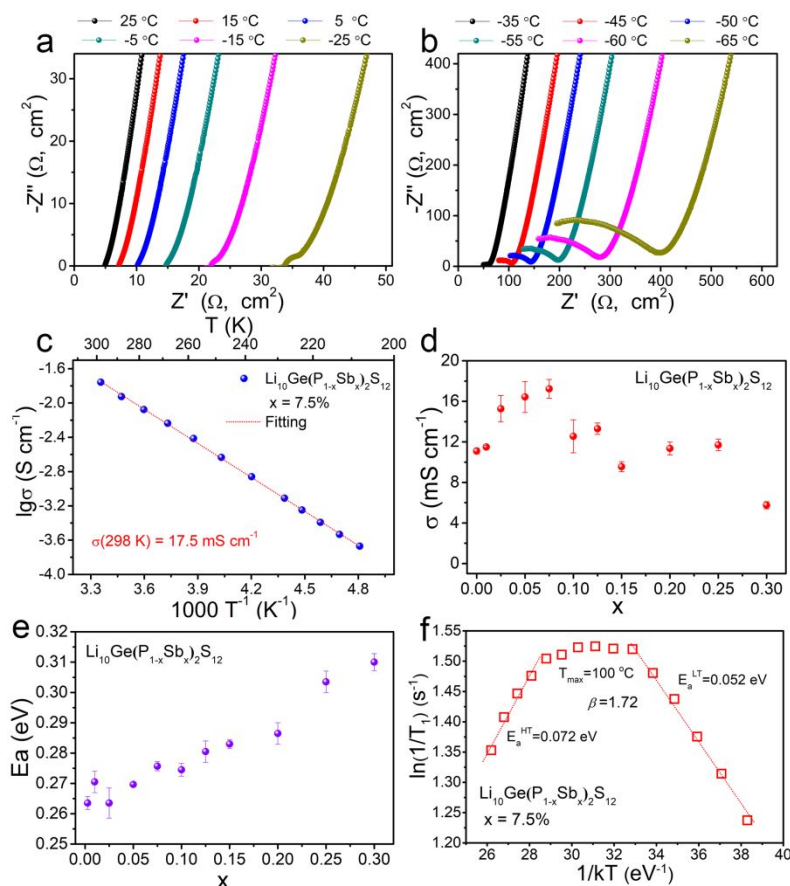


**Figure 3.** Ionic conductivity analysis of  $\text{Li}_{10}\text{Ge}(\text{P}_{1-x}\text{Sb}_x)_2\text{S}_{12}$  electrolytes. (a-b) Typical Nyquist plots of the  $\text{Li}_{10}\text{Ge}(\text{P}_{1-x}\text{Sb}_x)_2\text{S}_{12}$  ( $x = 7.5\%$ ) electrolyte in the temperature range of  $-65$  to  $25$  °C; (c) diffusivity calculated from experimentally measured ionic conductivity versus temperature. The redline is an Arrhenius fit to the data. The plotted conductivity represents the sum of the grain boundary and bulk conductivities.  $\text{Li}_{10}\text{Ge}(\text{P}_{1-x}\text{Sb}_x)_2\text{S}_{12}$  ( $x = 7.5\%$ ) exhibits an extremely high ionic conductivity of  $17.5 \text{ mS cm}^{-1}$  at  $25$  °C. (d) Ionic conductivities and (e) activation energies of  $\text{Li}_{10}\text{Ge}(\text{P}_{1-x}\text{Sb}_x)_2\text{S}_{12}$  electrolytes ( $0\% \leq x \leq 30\%$ ) at  $25$  °C, each composite were repeated two or three times. (f) Temperature dependence of the  $^7\text{Li}$  SLR rate of  $\text{Li}_{10}\text{Ge}(\text{P}_{0.925}\text{Sb}_{0.075})_2\text{S}_{12}$  measured in the laboratory frame of reference. The Larmor frequency ( $\omega_0/2\pi$ ) is  $155.248 \text{ MHz}$ .

The ionic conductivities of  $\text{Li}_{10}\text{Ge}(\text{P}_{1-x}\text{Sb}_x)_2\text{S}_{12}$  electrolytes were assessed using temperature-dependent electrochemical impedance spectroscopy (EIS) measurements with indium electrodes. Typical EIS profiles of the  $\text{Li}_{10}\text{Ge}(\text{P}_{1-x}\text{Sb}_x)_2\text{S}_{12}$  electrolyte ( $x = 7.5\%$ ) in the temperature range of  $-65$  to  $25$  °C are presented in Figure 3a,b. The EIS profiles of  $\text{Li}_{10}\text{Ge}(\text{P}_{0.925}\text{Sb}_{0.075})_2\text{S}_{12}$  obtained higher than  $-25$  °C ( $= 248 \text{ K}$ ) display only one obvious slope (Figure 3a), indicating the ultra-high ionic conductivity similar to other sulfide SSEs over  $10 \text{ mS cm}^{-1}$ .<sup>6-9</sup> The corresponded ionic conductivity was calculated based on the intercept of the slope on the x-axis. In contrast, the EIS profiles below  $-35$  °C ( $= 238 \text{ K}$ ) exhibit one extruded semicircle in the high-frequency region together with one slope in the low-frequency region. Thus, the EIS profiles were fitted with an equivalent circuit consisting of two parallel constant phase element/resistance (CPE/R) together with a CPE (Figure S7). The CPE/R at higher frequency corresponds to the bulk contribution, while the CPE/R in the middle frequency region corresponds to the grain-boundary contribution, and the CPE at lower frequency corresponds to the contributions of the In electrodes. The ionic conductivity was calculated by the total resistance of the bulk and grain-boundary value.

Figure 3c shows representative Arrhenius plots of  $\text{Li}_{10}\text{Ge}(\text{P}_{0.925}\text{Sb}_{0.075})_2\text{S}_{12}$  between  $-65$  to  $25$  °C.  $\text{Li}_{10}\text{Ge}(\text{P}_{0.925}\text{Sb}_{0.075})_2\text{S}_{12}$  exhibits an extremely high ionic conductivity of  $17.5 \text{ mS cm}^{-1}$  at  $25$  °C, which is higher than that of the  $12 \text{ mS cm}^{-1}$  ( $27$  °C) for  $\text{Li}_{10}\text{GeP}_2\text{S}_{12}$ ,<sup>6</sup> and is comparable to organic liquid electrolytes. Correspondingly, the activation energy is calculated to be  $0.274 \text{ eV}$ , and the electronic conductivity is determined to be  $\sim 1.5 \times 10^{-9} \text{ S cm}^{-1}$  (Figure S8). Typical Arrhenius plots of  $\text{Li}_{10}\text{Ge}(\text{P}_{0.975}\text{Sb}_{0.025})_2\text{S}_{12}$ ,  $\text{Li}_{10}\text{Ge}(\text{P}_{0.995}\text{Sb}_{0.005})_2\text{S}_{12}$ ,  $\text{Li}_{10}\text{Ge}(\text{P}_{0.9}\text{Sb}_{0.1})_2\text{S}_{12}$ ,  $\text{Li}_{10}\text{Ge}(\text{P}_{0.875}\text{Sb}_{0.125})_2\text{S}_{12}$ , and  $\text{Li}_{10}\text{Ge}(\text{P}_{0.8}\text{Sb}_{0.2})_2\text{S}_{12}$  are also presented in Figure S9-13. The ionic conductivities and activation energies for each composition of  $\text{Li}_{10}\text{Ge}(\text{P}_{1-x}\text{Sb}_x)_2\text{S}_{12}$  ( $0\% \leq x \leq 30\%$ ) were tested for repeatability and are summarized in Figure 3d,e. For Sb-substituted electrolytes with  $x$  in the range of 2.5-

12.5%, high room-temperature ionic conductivities of over  $12 \text{ mS cm}^{-1}$  can be achieved, demonstrating the improved  $\text{Li}^+$  diffusion caused by the introduction of Sb into  $\text{Li}_{10}\text{GeP}_2\text{S}_{12}$ . The corresponding activation energies ( $E_a$ ) presented in Figure 3e display an inverse trend compared to the ionic conductivity evolution when increasing the amount of Sb. The increased  $E_a$  might be related to the larger amount of impurities when the Sb substitution is too great, leading to the destruction of the pristine structure.

To acquire further information about the  $\text{Li}^+$  dynamics, spin-lattice relaxation rates (SLR) in a laboratory frame ( $1/T_1$ ) were measured for  $\text{Li}_{10}\text{Ge}(\text{P}_{0.925}\text{Sb}_{0.075})_2\text{S}_{12}$  at various temperatures as shown in Figure 3f. The  $^7\text{Li}$   $1/T_1$  relaxation maxima appeared at  $373 \text{ K}$  for a Larmor frequency of  $155.248 \text{ MHz}$  utilized in this work (Figure 3f), which is lower than the reported value of  $385 \text{ K}$  at  $155.3 \text{ MHz}$  reported for  $\text{Li}_{10}\text{GeP}_2\text{S}_{12}$  SSE,<sup>41</sup> indicating that the  $\text{Li}_{10}\text{Ge}(\text{P}_{0.925}\text{Sb}_{0.075})_2\text{S}_{12}$  SSE has a higher local  $\text{Li}^+$  mobility compared to the  $\text{Li}_{10}\text{GeP}_2\text{S}_{12}$  structure. Considering the case where the hopping frequency of  $\text{Li}^+$  is regarded to be equal to the Larmor frequency  $\omega_0$ ,<sup>42,43</sup> the Li-ion jump frequency  $1/\tau$  for the  $\text{Li}_{10}\text{Ge}(\text{P}_{0.925}\text{Sb}_{0.075})_2\text{S}_{12}$  SSE (at  $373 \text{ K}$ ) can be determined to be approximately  $9.75 \times 10^8 \text{ s}^{-1}$ . Furthermore, the  $\text{Li}_{10}\text{Ge}(\text{P}_{0.925}\text{Sb}_{0.075})_2\text{S}_{12}$  SSE reveals different slopes within the tested temperature range of  $303$ - $443 \text{ K}$ , which is related to the coexistence of different types of  $\text{Li}^+$  motion. The first one at the low-temperature flank has an activation energy of  $E_a^{\text{LT}} = 0.052 \text{ eV}$ , which may correspond to the ultrafast  $\text{Li}^+$  diffusion in the 1D tunnel along the  $c$  axis. The other slope at the high-temperature flank is characterized by  $E_a^{\text{HT}} = 0.072 \text{ eV}$ , which may be related to the fast  $\text{Li}^+$  diffusion in the plane perpendicular to the 1D tunnel along the  $ab$  plane. Thus, the asymmetry can be quantified to  $\beta = 1.72$ . The activation energies extracted by jump rates measured by NMR relaxometry SLR measurements are obviously lower than those determined by impedance tests. The results are reasonable since the NMR relaxometry SLR test is bulk selective, while the impedance tests are greatly influenced by bulk/grain boundary within the SSEs.<sup>44</sup>

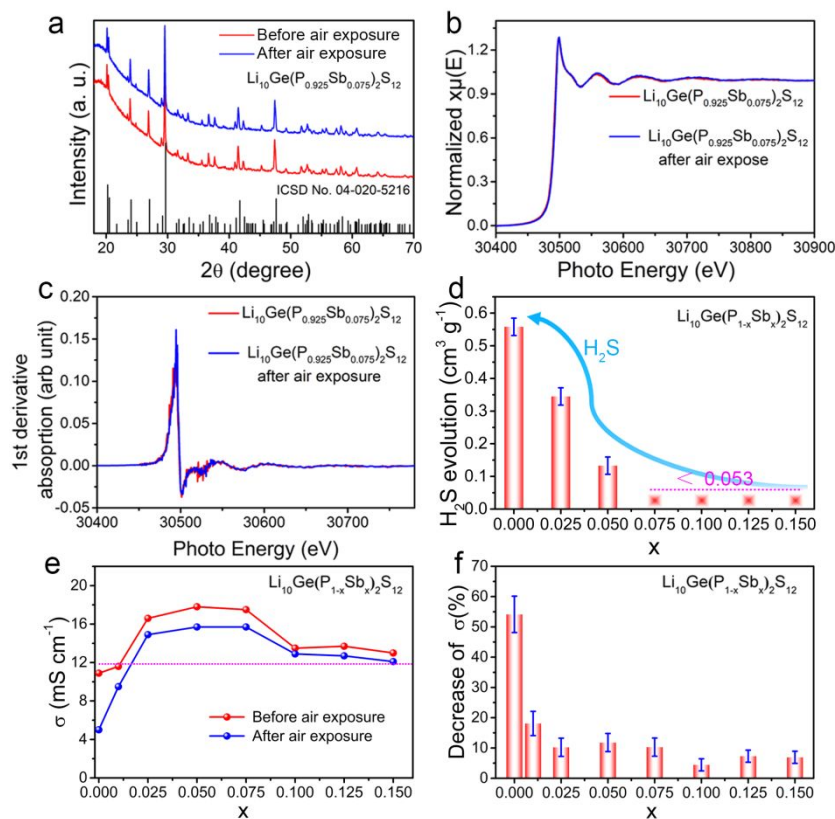


**Figure 4.** Characterization of the air-stability of  $\text{Li}_{10}\text{Ge}(\text{P}_{1-x}\text{Sb}_x)_2\text{S}_{12}$  with different compositions. (a) XRD pattern of  $\text{Li}_{10}\text{Ge}(\text{P}_{1-x}\text{Sb}_x)_2\text{S}_{12}$  ( $x = 7.5\%$ ) sample before and after air exposure. (b) Sb K-edge XAFS spectra and (c) corresponding first derivative spectra of  $\text{Li}_{10}\text{Ge}(\text{P}_{1-x}\text{Sb}_x)_2\text{S}_{12}$  ( $x = 7.5\%$ ) sample before and after air exposure. (d) Amount of  $\text{H}_2\text{S}$  gas generated from commercial  $\text{Li}_{10}\text{GeP}_2\text{S}_{12}$  and synthesized  $\text{Li}_{10}\text{Ge}(\text{P}_{0.925}\text{Sb}_{0.075})_2\text{S}_{12}$  powders. (e) Room-temperature ionic conductivities of  $\text{Li}_{10}\text{Ge}(\text{P}_{1-x}\text{Sb}_x)_2\text{S}_{12}$  ( $0\% \leq x \leq 15\%$ ) sample before and after air exposure. (f) The decrease of ionic conductivities of  $\text{Li}_{10}\text{Ge}(\text{P}_{1-x}\text{Sb}_x)_2\text{S}_{12}$  ( $0\% \leq x \leq 15\%$ ) after air exposure.

One typical disadvantage of sulfide SSEs is their instability towards air/moisture, which would lead to the generation of toxic  $\text{H}_2\text{S}$  gas and a significant reduction in the ionic conductivity of SSEs. Thus, good air/moisture tolerance is important for the development of practical SSEs at the industrial scale. Theoretically, the air/humidity instability of  $\text{Li}_{10}\text{GeP}_2\text{S}_{12}$  originates from the P-S bonds based on HSAB theory, where P-O bonds would preferentially form instead of the pristine P-S bonds. Thus, reducing the P content in  $\text{Li}_{10}\text{GeP}_2\text{S}_{12}$  should be helpful for improving the air/humidity stability.<sup>18,23</sup> To test the air stability,  $\text{Li}_{10}\text{Ge}(\text{P}_{1-x}\text{Sb}_x)_2\text{S}_{12}$  ( $0\% \leq x \leq 15\%$ ) powder samples were placed in a dry-room environment with humidity between 1-3% for over 24 h. As a comparison, the XRD patterns of the pristine  $\text{Li}_{10}\text{Ge}(\text{P}_{0.925}\text{Sb}_{0.075})_2\text{S}_{12}$  and the electrolyte after air-exposure are compared in Figure 4a. The two patterns are quite similar with no additional peaks or peak broadening observed, demonstrating the unchanged structure of  $\text{Li}_{10}\text{Ge}(\text{P}_{0.925}\text{Sb}_{0.075})_2\text{S}_{12}$ . The XRD pattern variations of other samples are presented in Figure S14-16. From the XRD results, it can be concluded that the  $\text{Li}_{10}\text{Ge}(\text{P}_{1-x}\text{Sb}_x)_2\text{S}_{12}$  SSEs with higher Sb content remain unchanged before and after air-exposure. Comparatively, the XRD pattern of commercial LGPS after air-exposure

presents obvious impurity peaks and peak splitting as shown in Figure S17. The stability of the  $\text{Li}_{10}\text{Ge}(\text{P}_{0.925}\text{Sb}_{0.075})_2\text{S}_{12}$  SSE was further proved by XAFS analysis (Figure 4b,c). The Sb K-edge spectra of pristine  $\text{Li}_{10}\text{Ge}(\text{P}_{0.925}\text{Sb}_{0.075})_2\text{S}_{12}$  and after air-exposure remain almost unchanged both spectral shape and energy position, further demonstrating its good air/humidity stability. Figure 4d shows the amounts of  $\text{H}_2\text{S}$  gas generated from the commercial  $\text{Li}_{10}\text{GeP}_2\text{S}_{12}$  and synthesized  $\text{Li}_{10}\text{Ge}(\text{P}_{1-x}\text{Sb}_x)_2\text{S}_{12}$  in a 1-3% humidity environment after 24 exposure. It can be seen that the amount of  $\text{H}_2\text{S}$  generation significantly decreased along with the increasing of Sb amount in  $\text{Li}_{10}\text{Ge}(\text{P}_{1-x}\text{Sb}_x)_2\text{S}_{12}$  SSEs. The results further confirmed that the synthesized  $\text{Li}_{10}\text{Ge}(\text{P}_{0.925}\text{Sb}_{0.075})_2\text{S}_{12}$  sample is more stable against humid air compared to the commercial  $\text{Li}_{10}\text{GeP}_2\text{S}_{12}$  based on the generation of  $\text{H}_2\text{S}$  gas.

The corresponding ionic conductivities of the  $\text{Li}_{10}\text{Ge}(\text{P}_{1-x}\text{Sb}_x)_2\text{S}_{12}$  before and after air-exposure at 25 °C were also tested (Figure 4e,f). The bare  $\text{Li}_{10}\text{GeP}_2\text{S}_{12}$  without any Sb substitution after air exposure exhibited a lower ionic conductivity of 5  $\text{mS cm}^{-1}$  compared to the pristine electrolyte (10.9  $\text{mS cm}^{-1}$ ), corresponding to a 54% decrease. In contrast, only 5-18% decrease was observed for

the  $\text{Li}_{10}\text{Ge}(\text{P}_{1-x}\text{Sb}_x)_2\text{S}_{12}$  samples. With a higher amount of Sb substitution, the room temperature ionic conductivities can achieve values as high as 12.1-15.7  $\text{mS cm}^{-1}$  (Arrhenius plots of typical  $\text{Li}_{10}\text{Ge}(\text{P}_{1-x}\text{Sb}_x)_2\text{S}_{12}$  samples before and after air exposure are shown in Figure S18-21). To the best of our knowledge, no reported sulfide-based SSEs can retain such

high ionic conductivities after air exposure.<sup>18,45-47</sup> The XRD,  $\text{H}_2\text{S}$  generation, and ionic conductivity tests provide evidence that introducing soft Sb acids that tend to bond with sulfur (soft base) rather than oxygen enables the significant improvement in the air stability of  $\text{Li}_{10}\text{GeP}_2\text{S}_{12}$ .

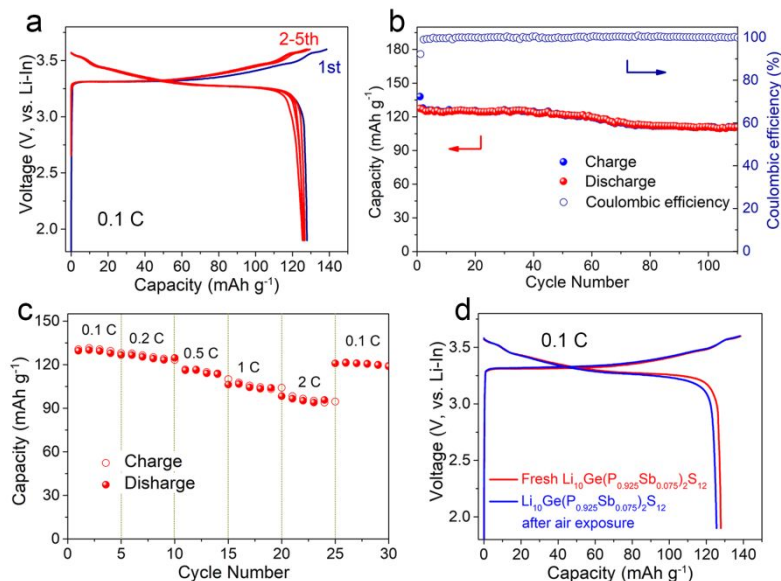


**Figure 5.** Electrochemical performance for the In/Li<sub>10</sub>Ge(P<sub>0.925</sub>Sb<sub>0.075</sub>)<sub>2</sub>S<sub>12</sub>/LiCoO<sub>2</sub> ASSB. (a) Typical charge and discharge curves for the In/Li<sub>10</sub>Ge(P<sub>0.925</sub>Sb<sub>0.075</sub>)<sub>2</sub>S<sub>12</sub>/LiCoO<sub>2</sub> cell at 0.1 C. (b,c) Cycling and rate performance of the In/Li<sub>10</sub>Ge(P<sub>0.925</sub>Sb<sub>0.075</sub>)<sub>2</sub>S<sub>12</sub>/LiCoO<sub>2</sub> cell. (d) Charge-discharge curves of In/Li<sub>10</sub>Ge(P<sub>0.925</sub>Sb<sub>0.075</sub>)<sub>2</sub>S<sub>12</sub>/LiCoO<sub>2</sub> cells with Li<sub>10</sub>Ge(P<sub>0.925</sub>Sb<sub>0.075</sub>)<sub>2</sub>S<sub>12</sub> before and after air exposure.

Similar to other sintered SSEs with super high ionic conductivities over  $10^{-2}$   $\text{S cm}^{-1}$  at room temperature,<sup>6-8</sup> a cold-pressed process was used to assemble ASSLBs using Li<sub>10</sub>Ge(P<sub>0.925</sub>Sb<sub>0.075</sub>)<sub>2</sub>S<sub>12</sub> as the SSEs, LiNbO<sub>x</sub> coated LiCoO<sub>2</sub> as the cathode (TEM image is shown in Figure S22), and In as the anode. Figure 5a shows the charge-discharge profiles recorded in the initial 5 cycles in the voltage range of 1.9-3.6 V vs. Li<sup>+</sup>/LiIn (2.5-4.2 V vs. Li<sup>+</sup>/Li) at 0.1 C (100 mA g<sup>-1</sup>) and 25 °C. The initial charge and discharge capacities are 138 and 128 mAh g<sup>-1</sup>, respectively, corresponding to an initial Coulombic Efficiency of 92.8%, which is similar to that of LiCoO<sub>2</sub> cathode in liquid cells. Subsequently, the discharge capacity stabilizes at 111 mAh g<sup>-1</sup> after 110 cycles at 0.1 C (Figure 5b) and high Coulombic efficiency over 99.9% is maintained during the cycling. The good capacity retention and highly reversible lithiation/delithiation indicate the formation of a beneficial and stable interface within the cathode composite layer. Furthermore, the ASSLBs based on Li<sub>10</sub>Ge(P<sub>0.925</sub>Sb<sub>0.075</sub>)<sub>2</sub>S<sub>12</sub> also present good rate capability, with capacities of 128, 125, 115, 107, and 98 mAh g<sup>-1</sup> observed at 0.1, 0.2, 0.5, 1, and 2 C, respectively (Figure 5c).

The performance of ASSLBs assembled with Li<sub>10</sub>Ge(P<sub>0.95</sub>Sb<sub>0.05</sub>)<sub>2</sub>S<sub>12</sub> SSEs after air-exposure was also tested, as shown in Figure 5d, S23. A high initial Coulombic Efficiency of 91% can be achieved and the charge-discharge curves overlap well with the ASSLBs based on fresh

Li<sub>10</sub>Ge(P<sub>0.925</sub>Sb<sub>0.075</sub>)<sub>2</sub>S<sub>12</sub> SSEs (Figure 5d). Capacity retention of 108 mAh g<sup>-1</sup> remained for over 50 cycles. To the best of our knowledge, this is the first report about ASSLBs based on sulfide SSEs after air exposure. The ASSLBs based Li<sub>10</sub>Ge(P<sub>0.925</sub>Sb<sub>0.075</sub>)<sub>2</sub>S<sub>12</sub> SSEs reported here demonstrate the practicality, feasibility and stability of the Li<sub>10</sub>Ge(P<sub>0.925</sub>Sb<sub>0.075</sub>)<sub>2</sub>S<sub>12</sub> SSEs for the real application of next-generation battery technology.

## CONCLUSION

In conclusion, Sb-substituted Li<sub>10</sub>Ge(P<sub>1-x</sub>Sb<sub>x</sub>)<sub>2</sub>S<sub>12</sub> SSEs were synthesized, and the structural variations/air stability was further investigated. Using Rietveld refinement against XRD, DFT calculations, and XAFS fitting, the detailed Sb substitution positions, and related unit cell parameters were confirmed. From theoretical and experimental results, it can be concluded that Sb substitutes in the (Ge,P)S<sub>4</sub> tetrahedra within the structure, leading to the opened framework and increased unit cell volume. Furthermore, the softer acidity of Sb compared to P results in stronger bonding between Sb<sup>3+</sup> and S<sup>2-</sup> with weaker interaction between S<sup>2-</sup> and Li<sup>+</sup>. Thus, the altered structure can better facilitate Li<sup>+</sup> migration as proved by the high ionic conductivity of  $17.3 \pm 0.9$   $\text{mS cm}^{-1}$ . More importantly, the Li<sub>10</sub>Ge(P<sub>1-x</sub>Sb<sub>x</sub>)<sub>2</sub>S<sub>12</sub> also shows outstanding stability toward air/moisture, structural stability and high ionic conductivity between 12.1-15.7  $\text{mS cm}^{-1}$  after air

exposure. The ASSLBs assembled with the air-exposed SSEs also exhibit electrochemical performances comparable to that of the pristine synthesized SSEs. This work demonstrates that reasonable substitution in  $\text{Li}_{10}\text{GeP}_2\text{S}_{12}$  can achieve highly air-stable sulfide SSEs as well as improved superionic conductivity. We believe that it is a great improvement toward designing more feasible SSEs for ASSLBs.

## ASSOCIATED CONTENT

**Supporting Information.** The Supporting Information is available free of charge via the Internet at <http://pubs.acs.org>. Detailed structures, tables, XRD patterns, Arrhenius plots, and  $\text{Li}^+$  conductivity tests of the as-prepared solid-state electrolytes.

## AUTHOR INFORMATION

### Corresponding Author

\* (X.S.) Email: [xsung@uwo.ca](mailto:xsung@uwo.ca)

### ORCID

Xueliang Sun: 0000-0003-0374-1245

Jianwen Liang: 0000-0003-4055-1301

Xiaona Li: 0000-0001-6713-2997

### Author Contributions

<sup>†</sup>J.L. and N.C. contributed equally to this work. J.L. and X.L. designed, performed the experiments on material synthesis, characterization, and battery testing. N.C., J.L., and M.B. contributed to the XAS experiments. C.Y. contributed to the NMR experiments. X.L. and C.W. contributed to the data analysis. R.L. helped with the SEM images. J.L., X.L., and K.A. prepared the manuscript. L.Z., S.Z., S.L., and H.H. participated in the discussion of the data. All authors discussed the results and commented on the manuscript. X.S. supervised the work.

### Notes

Any additional relevant notes should be placed here.

## ACKNOWLEDGMENT

This research was supported by Natural Sciences and Engineering Research Council of Canada (NSERC), GLABAT Solid-State Battery Inc., China Automotive Battery Research Institute Co. Ltd, Canada Research Chair Program (CRC), Canada Foundation for Innovation (CFI), Ontario Research Fund, the Canada Light Source at University of Saskatchewan (CLS), Canada MITACS fellow, and University of Western Ontario.

## REFERENCES

- (1) Zhao, Q.; Liu, X.; Stalin, S.; Khan, K.; Archer, L. A. Solid-state polymer electrolytes with in-built fast interfacial transport for secondary lithium batteries. *Nat. Energy* **2019**, *4*, 365-373.
- (2) Bachman, J. C.; Mui, S.; Grimaud, A.; Chang, H.-H.; Pour, N.; Lux, S. F.; Paschos, O.; Maglia, F.; Lupart, S.; Lamp, P. Inorganic solid-state electrolytes for lithium batteries: mechanisms and properties governing ion conduction. *Chem. Rev.* **2015**, *116*, 140.

- (3) Manthiram, A.; Yu, X.; Wang, S. Lithium battery chemistries enabled by solid-state electrolytes. *Nat. Rev. Mater.* **2017**, *2*, 16103.
- (4) Zhang, Z.; Shao, Y.; Lotsch, B.; Hu, Y.-S.; Li, H.; Janek, J.; Nazar, L. F.; Nan, C.-W.; Maier, J.; Armand, M. New horizons for inorganic solid state ion conductors. *Energy Environ. Sci.* **2018**, *11*, 1945.
- (5) Li, X.; Liang, J.; Chen, N.; Luo, J.; Adair, K. R.; Wang, C.; Banis, M. N.; Sham, T. K.; Zhang, L.; Zhao, S. Water - Mediated Synthesis of a Superionic Halide Solid Electrolyte. *Angew. Chem. Int. Ed.* **2019**, *58*, 16427-16432.
- (6) Kamaya, N.; Homma, K.; Yamakawa, Y.; Hirayama, M.; Kanno, R.; Yonemura, M.; Kamiyama, T.; Kato, Y.; Hama, S.; Kawamoto, K. A lithium superionic conductor. *Nat. Mater.* **2011**, *10*, 682.
- (7) Kato, Y.; Hori, S.; Saito, T.; Suzuki, K.; Hirayama, M.; Mitsui, A.; Yonemura, M.; Iba, H.; Kanno, R. High-power all-solid-state batteries using sulfide superionic conductors. *Nat. Energy* **2016**, *1*, 16030.
- (8) Kraft, M. A.; Ohno, S.; Zinkevich, T.; Koerver, R.; Culver, S. P.; Fuchs, T.; Senyshyn, A.; Indris, S.; Morgan, B. J.; Zeier, W. G. Inducing High Ionic Conductivity in the Lithium Superionic Argyrodites  $\text{Li}_{6+x}\text{P}_{1-x}\text{Ge}_x\text{S}_5\text{I}$  for All-Solid-State Batteries. *J. Am. Chem. Soc.* **2018**, *140*, 16330.
- (9) Sun, Y.; Suzuki, K.; Hori, S.; Hirayama, M.; Kanno, R. Superionic Conductors:  $\text{Li}_{10+\delta}[\text{Sn}_y\text{Si}_{11-y}]_{14}\delta\text{P}_2-\delta\text{S}_{12}$  with a  $\text{Li}_0\text{GeP}_2\text{S}_{12}$ -type Structure in the  $\text{Li}_3\text{PS}_4\text{-Li}_4\text{SnS}_4\text{-Li}_4\text{SiS}_4$  Quasi-ternary System. *Chem. Mater.* **2017**, *29*, 5858.
- (10) Nazar, L.; Adeli, P.; Bazak, J. D.; Park, K.-H.; Kochetkov, I.; Huq, A.; Goward, G. Boosting solid - state diffusivity and conductivity in lithium superionic argyrodites by halide substitution. *Angew. Chem. Int. Ed.* **2019**, *58*, 8681-8686.
- (11) Li, X.; Liang, J.; Luo, J.; Wang, C.; Li, X.; Sun, Q.; Li, R.; Zhang, L.; Yang, R.; Lu, S. High - Performance Li - SeS<sub>x</sub> All - Solid - State Lithium Batteries. *Adv. Mater.* **2019**, *31*, 1808100.
- (12) Gao, Y.; Wang, D.; Li, Y. C.; Yu, Z.; Mallouk, T. E.; Wang, D. Salt - Based Organic - Inorganic Nanocomposites: Towards A Stable Lithium Metal/ $\text{Li}_0\text{GeP}_2\text{S}_{12}$  Solid Electrolyte Interface. *Angew. Chem. Int. Ed.* **2018**, *57*, 13608.
- (13) Wang, C.; Adair, K. R.; Liang, J.; Li, X.; Sun, Y.; Li, X.; Wang, J.; Sun, Q.; Zhao, F.; Lin, X. et al. Solid-State Plastic Crystal Electrolytes: Effective Protection Interlayers for Sulfide-Based All-Solid-State Lithium Metal Batteries. *Adv. Fun. Mater.* **2019**, *29*, 1900392.
- (14) Miura, A.; Rosero-Navarro, N. C.; Sakuda, A.; Tadanaga, K.; Phuc, N. H.; Matsuda, A.; Machida, N.; Hayashi, A.; Tatsumisago, M. Liquid-phase syntheses of sulfide electrolytes for all-solid-state lithium battery. *Nat. Rev. Chem.* **2019**, *3*, 189-198.
- (15) Wang, Y.; Liu, Z.; Zhu, X.; Tang, Y.; Huang, F. Highly lithium-ion conductive thio-LISICON thin film processed by low-temperature solution method. *J. Power Sources* **2013**, *224*, 225.
- (16) Sahu, G.; Lin, Z.; Li, J.; Liu, Z.; Dudney, N.; Liang, C. Air-stable, high-conduction solid electrolytes of arsenic-substituted  $\text{Li}_4\text{SnS}_4$ . *Energy Environ. Sci.* **2014**, *7*, 1053.
- (17) Pearson, R. G. Hard and soft acids and bases, HSAB, part 1: Fundamental principles. *J. Chem. Edu.* **1968**, *45*, 581.
- (18) Wang, H.; Chen, Y.; Hood, Z. D.; Sahu, G.; Pandian, A. S.; Keum, J. K.; An, K.; Liang, C. An Air-Stable  $\text{Na}_3\text{SbS}_4$  Superionic Conductor Prepared by a Rapid and Economic Synthetic Procedure. *Angew. Chem. Int. Ed.* **2016**, *55*, 8551.
- (19) Zhang, B. W.; Sheng, T.; Wang, Y. X.; Chou, S.; Davey, K.; Dou, S. X.; Qiao, S. Z. Long - Life Room - Temperature Sodium - Sulfur Batteries by Virtue of Transition - Metal - Nanocluster - Sulfur Interactions. *Angew. Chem. Int. Ed.* **2019**, *58*, 1484.

- (20) Ye, C.; Jiao, Y.; Jin, H.; Slattery, A. D.; Davey, K.; Wang, H.; Qiao, S. Z. 2D MoN - VN Heterostructure To Regulate Polysulfides for Highly Efficient Lithium - Sulfur Batteries. *Angew. Chem. Int. Ed.* **2018**, *57*, 16703.
- (21) Wang, Y.; Lü, X.; Zheng, C.; Liu, X.; Chen, Z.; Yang, W.; Lin, J.; Huang, F. Chemistry Design Towards a Stable Sulfide - based Superionic Conductor Li<sub>4</sub>Cu<sub>8</sub>Ge<sub>3</sub>S<sub>12</sub>. *Angew. Chem. Int. Ed.* **2019**, *58*, 7673-7677.
- (22) Ramos, E. P.; Zhang, Z.; Assoud, A.; Kaup, K.; Lalère, F.; Nazar, L. F. Correlating Ion Mobility and Single Crystal Structure in Sodium-Ion Chalcogenide-Based Solid State Fast Ion Conductors: Na<sub>11</sub>Sn<sub>2</sub>PnS<sub>12</sub> (Pn= Sb, P). *Chem. Mater.* **2018**, *30*, 7413.
- (23) Kimura, T.; Kato, A.; Hotehama, C.; Sakuda, A.; Hayashi, A.; Tatsumisago, M. Preparation and characterization of lithium ion conductive Li<sub>3</sub>SbS<sub>4</sub> glass and glass-ceramic electrolytes. *Solid State Ionics* **2019**, *333*, 45.
- (24) Banerjee, A.; Park, K. H.; Heo, J. W.; Nam, Y. J.; Moon, C. K.; Oh, S. M.; Hong, S. T.; Jung, Y. S. Na<sub>3</sub>SbS<sub>4</sub>: A Solution Processable Sodium Superionic Conductor for All - Solid - State Sodium - Ion Batteries. *Angew. Chem. Int. Ed.* **2016**, *55*, 9634.
- (25) Tian, Y.; Sun, Y.; Hannah, D. C.; Xiao, Y.; Liu, H.; Chapman, K. W.; Bo, S.-H.; Ceder, G. Reactivity-Guided Interface Design in Na Metal Solid-State Batteries. *Joule* **2019**, *3*, 1037-1050.
- (26) Shannon, R. D. Revised effective ionic radii and systematic studies of interatomic distances in halides and chalcogenides. *Acta crystallographica section A: crystal physics, diffraction, theoretical and general crystallography* **1976**, *32*, 751.
- (27) Bernges, T.; Culver, S. P.; Minafra, N.; Koerver, R.; Zeier, W. G. Competing Structural Influences in the Li Superionic Conducting Argyrodites Li<sub>6</sub>PS<sub>5-x</sub>SexBr (0 ≤ x ≤ 1) upon Se Substitution. *Inorg. Chem.* **2018**, *57*, 13920.
- (28) Krauskopf, T.; Muy, S.; Culver, S. P.; Ohno, S.; Delaire, O.; Shao-Horn, Y.; Zeier, W. G. Comparing the Descriptors for Investigating the Influence of Lattice Dynamics on Ionic Transport Using the Superionic Conductor Na<sub>3</sub>PS<sub>4-x</sub>Se x. *J. Am. Chem. Soc.* **2018**, *140*, 14464.
- (29) Jiang, D.; Chen, N.; Sheng, W. AIP Conference Proceedings, **2007**; p 800.
- (30) Wang, B.; Zhao, Y.; Banis, M. N.; Sun, Q.; Adair, K. R.; Li, R.; Sham, T.-K.; Sun, X. Atomic layer deposition of lithium niobium oxides as potential solid-state electrolytes for lithium-ion batteries. *ACS Appl. Mater. Interfaces* **2018**, *10*, 1654.
- (31) Li, X.; Ren, Z.; Norouzi Banis, M.; Deng, S.; Zhao, Y.; Sun, Q.; Wang, C.; Yang, X.; Li, W.; Liang, J. Unravelling the Chemistry and Microstructure Evolution of a Cathodic Interface in Sulfide-Based All-Solid-State Li-Ion Batteries. *ACS Energy Lett.* **2019**, *4*, 2480.
- (32) Kuhn, A.; Köhler, J.; Lotsch, B. V. Single-crystal X-ray structure analysis of the superionic conductor Li<sub>10</sub>GeP<sub>2</sub>S<sub>12</sub>. *Phys. Chem. Chem. Phys.* **2013**, *15* (28), 11620.
- (33) Rodríguez-Carvajal, J. Recent advances in magnetic structure determination by neutron powder diffraction. *Physica B: Condensed Matter* **1993**, *192*, 55.
- (34) Favre-Nicolin, V.; Černý, R. FOX, free objects for crystallography: a modular approach to ab initio structure determination from powder diffraction. *J. App. Crystal.* **2002**, *35*, 734.
- (35) Weber, D. A.; Senyshyn, A.; Weldert, K. S.; Wenzel, S.; Zhang, W.; Kaiser, R.; Berendts, S.; Janek, J. r.; Zeier, W. G. Structural insights and 3D diffusion pathways within the lithium superionic conductor LioGeP<sub>2</sub>S<sub>12</sub>. *Chem. Mater.* **2016**, *28*, 5905.
- (36) Mo, Y.; Ong, S. P.; Ceder, G. First principles study of the LioGeP<sub>2</sub>S<sub>12</sub> lithium super ionic conductor material. *Chem. Mater.* **2011**, *24*, 15.
- (37) Rehr, J. J.; Albers, R. C. Theoretical approaches to x-ray absorption fine structure. *Rev. Mod. Phys.* **2000**, *72* (3), 621.
- (38) Ravel, B.; Newville, M. ATHENA, ARTEMIS, HEPHAESTUS: data analysis for X-ray absorption spectroscopy using IFEFFIT. *J. Synchrotron Radiat.* **2005**, *12* (4), 537.
- (39) Ressler, T. WinXAS: A new software package not only for the analysis of energy-dispersive XAS data. *J. Phys. IV* **1997**, *7*, C2-269-C2-270.
- (40) Joly, Y. X-ray absorption near-edge structure calculations beyond the muffin-tin approximation. *Phys. Rev. B* **2001**, *63*, 125120.
- (41) Liang, X.; Wang, L.; Jiang, Y.; Wang, J.; Luo, H.; Liu, C.; Feng, J. In-channel and In-plane Li ion diffusions in the superionic conductor LioGeP<sub>2</sub>S<sub>12</sub> Probed by solid-state NMR. *Chem. Mater.* **2015**, *27*, 5503.
- (42) Kuhn, A.; Narayanan, S.; Spencer, L.; Goward, G.; Thangadurai, V.; Wilkening, M. Li self-diffusion in garnet-type Li<sub>7</sub>La<sub>3</sub>Zr<sub>2</sub>O<sub>12</sub> as probed directly by diffusion-induced Li 7 spin-lattice relaxation NMR spectroscopy. *Phys. Rev. B* **2011**, *83*, 094302.
- (43) Wilkening, M.; Heitjans, P. From Micro to Macro: Access to Long-Range Li+ Diffusion Parameters in Solids via Microscopic 6,7Li Spin-Alignment Echo NMR Spectroscopy. *ChemPhysChem* **2012**, *13*, 53.
- (44) Wang, H.; Yu, C.; Ganapathy, S.; van Eck, E. R.; van Eijck, L.; Wagemaker, M. A lithium argyrodite Li<sub>6</sub>PS<sub>5</sub>Cl<sub>0.5</sub>Br<sub>0.5</sub> electrolyte with improved bulk and interfacial conductivity. *J. Power Sources* **2019**, *412*, 29.
- (45) Banerjee, A.; Park, K. H.; Heo, J. W.; Nam, Y. J.; Moon, C. K.; Oh, S. M.; Hong, S. T.; Jung, Y. S. Na<sub>3</sub>SbS<sub>4</sub>: A Solution Processable Sodium Superionic Conductor for All - Solid - State Sodium - Ion Batteries. *Angew. Chem. Int. Ed.* **2016**, *128*, 9786-9790.
- (46) Park, K. H.; Oh, D. Y.; Choi, Y. E.; Nam, Y. J.; Han, L.; Kim, J. Y.; Xin, H.; Lin, F.; Oh, S. M.; Jung, Y. S. Solution - Processable Glass Lil - Li<sub>4</sub>SnS<sub>4</sub> Superionic Conductors for All - Solid - State Li - Ion Batteries. *Adv. Mater.* **2016**, *28*, 1874.
- (47) Yu, Z.; Shang, S. L.; Seo, J. H.; Wang, D.; Luo, X.; Huang, Q.; Chen, S.; Lu, J.; Li, X.; Liu, Z. K. Exceptionally High Ionic Conductivity in Na<sub>3</sub>PO<sub>3.62</sub>AsO<sub>3.38</sub>S<sub>4</sub> with Improved Moisture Stability for Solid - State Sodium - Ion Batteries. *Adv. Mater.* **2017**, *29*, 1605561.

## Table of Contents

